Direct observation of 3D atomic packing in monatomic amorphous materials

Yakun Yuan[1*], Dennis S. Kim[1*], Jihan Zhou[1*], Dillan J. Chang[1], Fan Zhu[1], Yasutaka Nagaoka[2], Yao Yang[1], Minh Pham[3], Stanley J. Osher[3], Ou Chen[2], Peter Ercius[4], Andreas K. Schmid[4], Jianwei Miao[1†]

[1]Department of Physics & Astronomy and California NanoSystems Institute, University of California, Los Angeles, CA 90095, USA. [2]Department of Chemistry, Brown University, Providence, RI 02912, USA. [3]Department of Mathematics, University of California, Los Angeles, CA 90095, USA. [4]National Center for Electron Microscopy, Molecular Foundry, Lawrence Berkeley National Laboratory, Berkeley, CA 94720, USA.

[*]These authors contributed equally to this work.

[†]Correspondence and requests for materials should be addressed to J.M. (miao@physics.ucla.edu).

Liquids and solids are two fundamental states of matter. Although the structure of crystalline solids has long been solved by crystallography, our understanding of the 3D atomic structure of liquids and amorphous materials remained speculative. In 1952, Frank hypothesized that icosahedral order is the prevalent atomic motif in monatomic liquids[1]. Over the past six decades, there have been a great deal of experimental, computational and theoretical studies to understand the structure of liquids and amorphous materials[2-15]. A polytetrahedral packing model was proposed to explain the 3D atomic structure of monatomic liquids and amorphous materials[16], in which icosahedral order is a key feature. The icosahedral order has also been found to play an important role in the structure of metallic glasses and quasicrystals[17-20]. Here we advance atomic electron tomography[21,22] to determine for the first time the 3D atomic positions in monatomic amorphous materials, including a Ta thin film and two Pd nanoparticles.

Despite the different chemical composition and synthesis methods, we observe that pentagonal bipyramids are the most abundant atomic motifs in these amorphous materials. Contrary to the traditional understanding, the pentagonal bipyramids do not assemble full icosahedra, but are closely connected with each other to form networks that extend to medium-range scale. Our molecular dynamic simulations, coupled with experimental results, further reveal that the 3D atomic structure of monatomic liquids is similar to the experimental amorphous material. Moreover, we find that the pentagonal bipyramid networks, prevalent in monatomic liquids, rapidly grow in size and form a fraction of full icosahedra during the quench from a liquid to a metallic glass state, providing a possible new picture of structural evolution through the glass transition.

The atomic electron tomography (AET) experiments were conducted with an aberration corrected scanning transmission electron microscope in annular dark-field mode. Tomographic tilt series were acquired from an amorphous Ta thin film and two Pd nanoparticles (Extended Data Table 1 and Extended Data Figs. 1 and 2), which were synthesized by physical vapor deposition and colloidal chemistry with ligand engineering, respectively (Methods). Images taken before, during and after the acquisition of each tilt series indicate a minimal change of the sample structure throughout the experiment (Extended Data Fig. 3a-g). After image pre-processing, each tilt series was reconstructed by a real space iterative algorithm and the 3D coordinates of individual atoms were traced and refined to produce an experimental atomic model (Methods). Compared to nanoparticles[23-25], the AET reconstruction of thin films is more challenging as the projections at different tilt angles contain different volumes of the thin film (Extended Data Fig. 3a). We implemented a powerful reconstruction algorithm (Methods) to solve this problem and determined the 3D atomic coordinates in the amorphous Ta thin film. The precision of the 3D atomic coordinates was validated to be 18 picometers (Extended Data Fig. 3h-j) (Methods).

Figure 1a, b and Extended Data Fig. 4a, b show the experimental 3D atomic model of the Ta film and two Pd nanoparticles (named Pd_1 and Pd_2), respectively, where the amorphous rings are observed by taking the Fourier transform of the experimental images at 0° tilt (insets). To quantify the disorder, we calculated the bond orientational order parameter for all the atoms[26] (Extended Data Fig. 4c-e, Methods), and found that a small fraction of atoms form crystal nuclei on the surface of the amorphous materials (gray atoms in Fig. 1a, b, Extended Data Fig. 4a, Supplementary Video 1 and 2). By excluding these nuclei, we computed the radial distribution functions (RDFs) for the disordered atoms (Fig. 1c). After normalization with the Ta and Pd atom size, the RDFs show similar shapes despite the different chemical composition and synthesis methods of the samples. As a comparison, the RDF of a Ta liquid obtained by molecular dynamics is plotted as a dotted curve in Fig. 1c, and its peak and valley positions agree with those of the experimental RDFs of the amorphous materials. Based on the first valley in the RDFs, we quantified the local atomic packing using the Voronoi tessellation[4]. This method characterizes each local polyhedron around a center atom by calculating a Voronoi index, $<n_3, n_4, n_5, n_6>$, where n_i denotes the number of i-edge faces (Methods). From the Voronoi indices, we determined the average coordination number of the Ta, Pd_1 and Pd_2 sample to be 11.7, 11.2 and 11.1, respectively, which agree with that of monatomic liquids (12±1) measured by diffraction experiments[27]. Figure 1d shows the 11 most populated Voronoi polyhedra in the samples. We found that icosahedra with <0,0,12,0> account for only 0.6%, 0.4% and 0.4%, while distorted icosahedra with <0,1,10,2>, <0,2,8,2> and <0,2,8,1> constitute 9.5%, 10.1% and 10.1% in the Ta, Pd_1 and Pd_2 sample, respectively. In contrast, among all the faces in the Voronoi polyhedra (Extended Data Fig. 4f), five-edged faces are the most abundant (44.8%, 46.1% and 46.2%, respectively), indicating that the majority of five-edge faces do not form icosahedra.

Next, we analysed the polytetrahedral packing in the amorphous materials (Methods). We quantified the shape of all tetrahedra in the samples by a distortion parameter[13,28], defined as $\delta = e_{max}/\, e_{avg} - 1$, where e_{max} and e_{avg} are the maximum and average edge length of the tetrahedron, respectively. The fraction of tetrahedra in the amorphous samples as a function of δ is shown in Extended Data Fig. 4g-i (green curves). With $\delta > 0.2$, more than 96.8% of the atoms in the samples form tetrahedra. By sharing faces, these tetrahedra constitute four main motifs: triplets, quadrilateral, pentagonal and hexagonal bipyramids (Fig. 2a). We represent the four motifs with three-, four-, five- and six-fold skeletons by connecting the centroids of the tetrahedra (colored lines in Fig. 2a). Figure 2b and Extended Data Fig. 4g-i show the fraction of the four motifs as a function of δ. With $\delta < 0.2$, the tetrahedra are not fully packed in 3D space leading to a dominant fraction of triplets. As δ increases, quadrilateral, pentagonal and hexagonal bipyramids become more abundant, while triplets significantly decrease. In the following analysis, we chose δ = 0.255, which was used in previous mathematical and numerical simulation studies[13,28]. Figure 2c shows the population of the four motifs in the three samples, indicating that pentagonal bipyramids are the most abundant atomic motif. This observation is consistent with the Voronoi tessellation result (Extended Data Fig. 4f), and can be explained that pentagonal bipyramids require less distortion to pack than the other motifs[16]. Since a tetrahedron and a pentagonal bipyramid represent the densest packing of four and seven atoms, respectively, we correlated the polytetrahedral packing with the local mass density of the amorphous materials (Methods) and observed that 3D local mass density heterogeneity is strongly related to the atomic packing of the four motifs in all three samples (Fig. 2d and Extended Data Fig. 5).

As pentagonal bipyramids are the most abundant atomic motifs, we quantified their 3D packing in the amorphous materials. A fraction of bipyramids link to each other by sharing vertices or edges of the five-fold skeletons (Fig. 3a, b). Figure 3c and Extended Data Fig. 6

show the fraction of pentagonal bipyramids as a function of the number of vertex- and edge-sharing neighbours. We found that 63.5% of bipyramids do not share any vertices with each other in the three samples, but the majority of them (72.5%) share at least one edge with their neighbours. Figure 3d and e shows two pentagonal bipyramid clusters with the most vertex- and edge-sharing neighbours, respectively, where a larger cluster is formed by edge-sharing. These results indicate that edge-sharing of the five-fold skeletons is a dominant feature in the packing of pentagonal bipyramids. We then investigated if these pentagonal bipyramids form icosahedra. A full icosahedron requires the tight packing of 12 pentagonal bipyramids by edge-sharing. But we observed only partial icosahedra, where the maximum number of packed pentagonal bipyramids is 10, 9 and 10 for the Ta, Pd_1 and Pd_2 sample, respectively (Fig. 3f). This result does not contradict the observation of 0.4% icosahedra among all Voronoi polyhedra in the three samples as the icosahedra in the Voronoi tessellation have a larger distortion with $\delta > 0.255$ (Extended Data Fig. 7a-c).

Instead of assembling full icosahedra, the pentagonal bipyramids with edge-sharing skeletons form networks that extend to the nanoscale in all three samples. Figure 3g shows a representative pentagonal bipyramid network (PBN), which consists of five partial icosahedra. The histogram of the PBNs as a function their size and length is shown in Fig. 3h and Extended Data Figs. 7d-i. The largest PBN was found in the Ta film, which consists of 135 pentagonal bipyramids formed by 165 atoms with an end-to-end length of 2.83 nm (Fig. 3i). The five largest PBNs in the Ta, Pd_1 and Pd_2 sample are shown in Extended Data Fig. 8, respectively. Compared with the networks formed by quadrilateral and hexagonal bipyramids, the PBNs not only are more abundant, but also have a larger size in all three samples (Extended Data Fig. 7d-i), indicating the PBNs are dominant in monatomic amorphous materials.

To investigate if PBNs are prevalent in other amorphous systems such as liquids and metallic glasses, we employed molecular dynamics simulations using the large-scale

atomic/molecular massively parallel simulator (Methods). A bulk Ta solid was melted at 5200 K, quenched at a cooling rate of 10^{13} K/s and brought to equilibrium at 300 K. The RDFs of the Ta structures at varying temperatures are shown in Extended Data Fig. 9a. At 5200 K, the RDF of the Ta liquid resembles those of experimentally measured amorphous materials in terms of the peak and valley positions (dotted curve in Fig. 1c). At 300 K, the splitting of the 2nd and 3rd peaks in the RDF indicates the formation of the Ta metallic glass[14,17] (arrows in Extended Data Fig. 9a). By analysing the polytetrahedral packing of these Ta structures with $\delta = 0.255$, we found that pentagonal bipyramids are the most abundant atomic motifs across the entire temperature range and their population dramatically increases with the decrease of the temperature (Fig. 4a). The pentagonal bipyramids constitute partial or full icosahedra depending on the temperature. At 5200 K, we observed PBNs and only partial icosahedra in the Ta liquid (Fig. 4b, c and Extended Data Fig. 9b-f). These PBNs extend to the nanoscale and resemble those found in the experimental Ta, Pd_1 and Pd_2 sample (Fig. 3h, i and Extended Data Fig. 7d-i). With the decrease of the temperature, a small fraction (1.4%) of full icosahedra are assembled from the pentagonal bipyramids and the PBNs grow in size (Fig. 4b, d and Extended Data Fig. 9g-i). At 300 K, the fraction of full icosahedra is increased to 12.6% and a huge PBN is formed across the entire Ta metallic glass (Fig. 4b, e and Extended Data Fig. 9i).

Our experimental results, coupled with molecular dynamics simulations, provide a fundamental insight into the 3D atomic packing of monatomic amorphous materials and liquids. The RDF, coordination number and 3D atomic arrangement of the monatomic liquid resemble those of the experimental amorphous materials synthesized by different methods. These observations pose a deep question on why these monatomic amorphous materials and liquids, as two different states of matter, have similar 3D atomic structures. Moreover, we find that, although pentagonal bipyramids are prevalent in the monatomic amorphous materials and liquids, they do not form full icosahedra, but instead arrange into nanoscale PBNs. During the

quench from a liquid to metallic glass state, the PBNs quickly grow in size and form a small fraction of full icosahedra, indicating an important role of the PBNs during the glass transition. Looking forward, the ability to determine the 3D atomic structure of amorphous thin films is expected to greatly expand the applicability of AET to a broad range of technologically relevant materials[29]. Furthermore, our experimental method and results could have an important impact on other fields, ranging from the direct determination of the 3D atomic structure of quasicrystals[19,20] to the study of the amorphous-crystalline phase transition and glass transition at the atomic scale[30].

References:

1. Frank, F. C. Supercooling of liquids. *Proc. R. Soc. London. Ser. A. Math. Phys. Sci.* 215, 43–46 (1952).
2. Bernal, J. D. A geometrical approach to the structure of liquids. *Nature* **183**, 141–147(1959).
3. Scott, G. D. Packing of Spheres: Packing of Equal Spheres. *Nature* **188**, 908–909(1960).
4. Finney, J. L. Random Packings and the Structure of Simple Liquids. I. The Geometry of Random Close Packing. *Proc. Roy Soc. Lond. Ser. A - Math. Phys. Sci.* **319**, 479-493 (1970).
5. Nelson, D. R. Order, frustration, and defects in liquids and glasses. *Phys. Rev. B.* **28**, 5515–5535 (1983).
6. Jonsson, H. & Andersen, H. C. Icosahedral Ordering in the Lennard-Jones Liquid and Glass. *Phys. Rev. Lett.* **60**, 2295-2298 (1988).
7. Reichert, H. et al. Observation of Five-Fold Local Symmetry in Liquid Lead. *Nature* **408**, 839-841 (2000).
8. Spaepen, F. Five-fold symmetry in liquids. *Nature* **408**, 781-782 (2000).
9. Kelton, K. F. *et al*. First X-Ray Scattering Studies on Electrostatically Levitated Metallic Liquids: Demonstrated Influence of Local Icosahedral Order on the Nucleation Barrier. *Phys. Rev. Lett.* **90**, 195504 (2003).

10. Schenk, T., Holland-Moritz, D., Simonet, V., Bellissent, R. & Herlach, D. M. Icosahedral Short-Range Order in Deeply Undercooled Metallic Melts. *Phys. Rev. Lett.* **89**, 075507 (2002).
11. Jakse, N. & Pasturel, A. Local Order of Liquid and Supercooled Zirconium by *Ab Initio* Molecular Dynamics. *Phys. Rev. Lett.* **91**, 195501 (2003).
12. Di Cicco, A., Trapananti, A., Faggioni, S. & Filipponi, A. Is There Icosahedral Ordering in Liquid and Undercooled Metals? *Phys. Rev. Lett.* **91**, 1–4 (2003).
13. Anikeenko, A. V. & Medvedev, N. N. Polytetrahedral Nature of the Dense Disordered Packings of Hard Spheres. *Phys. Rev. Lett.* **98**, 235504 (2007).
14. Zhong, L., Wang, J., Sheng, H., Zhang, Z. & Mao, S. X. Formation of monatomic metallic glasses through ultrafast liquid quenching. *Nature* **512**, 177-180 (2014).
15. Tanaka, H., Tong, H., Shi, R. & Russo, J. Revealing key structural features hidden in liquids and glasses. *Nat. Rev. Phys*. **1**, 333–348 (2019).
16. Nelson, D. R. & Spaepen, F. Polytetrahedral Order in Condensed Matter. *Solid Stat. Phys*. **42**, 1–90 (1989).
17. Cheng, Y. Q. & Ma, E. Atomic-level structure and structure–property relationship in metallic glasses. *Prog. Mater. Sci.* **56**, 379–473 (2011).
18. Hirata, A. *et al*. Geometric Frustration of Icosahedron in Metallic Glasses. *Science* **341**, 376-9 (2013).
19. Shechtman, D., Blech, I., Gratias, D. & Cahn, J. Metallic Phase with Long-Range Orientational Order and No Translational Symmetry. *Phys. Rev. Lett.* **53**, 1951–1953 (1984).
20. Levine, D. & Steinhardt, P. J. Quasicrystals: A New Class of Ordered Structures. *Phys. Rev. Lett*. **53**, 2477-2480 (1984).
21. Miao, J., Ercius, P. & Billinge, S. J. L. Atomic electron tomography: 3D structures without crystals. *Science* **353**, aaf2157 (2016).
22. Yang, Y. *et al*. Determining the three-dimensional atomic structure of an amorphous solid. arXiv:2004.02266v1.

23. Scott, M. C. *et al.* Electron tomography at 2.4-ångström resolution. *Nature*. **483**, 444–447 (2012).
24. Chen, C. C. *et al*. Three-dimensional imaging of dislocations in a nanoparticle at atomic resolution. *Nature*. **496**, 74–77 (2013).
25. Zhou, J. *et al*. Observing crystal nucleation in four dimensions using atomic electron tomography. *Nature*. **570**, 500–503 (2019).
26. Steinhardt, P. J., Nelson, D. R. & Ronchetti, M. Bond-orientational order in liquids and glasses. *Phys. Rev. B* **28**, 784-805 (1983).
27. Lee, G. W. *et al.* Difference in Icosahedral Short-Range Order in Early and Late Transition Metal Liquids. *Phys. Rev. Lett*. **93**, 037802 (2004).
28. Hales, T. C. A proof of the Kepler conjecture. *Ann. Math.* **162**, 1065–1185 (2005).
29. Ohring, M. *Materials Science of Thin Films* (Academic Press, 2nd ed., 2001).
30. Debenedetti, P. G. & Stillinger, F. H. Supercooled liquids and the glass transition. *Nature* **410**, 259-267 (2001).

Acknowledgements We thanks Jim Ciston for help with data acquisition and Xuezeng Tian with data analysis. Funding: This work was primarily supported by the US Department of Energy (DOE), Office of Science, Basic Energy Sciences, Division of Materials Sciences and Engineering under award DE-SC0010378 (experiments) and by STROBE: a National Science Foundation (NSF) Science and Technology Center under award DMR-1548924 (data analysis). It was also partially supported by the NSF DMREF program under award DMR-1437263, and the Army Research Office MURI program under grant no. W911NF-18-1-0431. The ADF-STEM imaging with TEAM I was performed at the Molecular Foundry, which is supported by the Office of Science, Office of Basic Energy Sciences of the US DOE under contract no. DE-AC02-05CH11231.

Figures and Figure legends

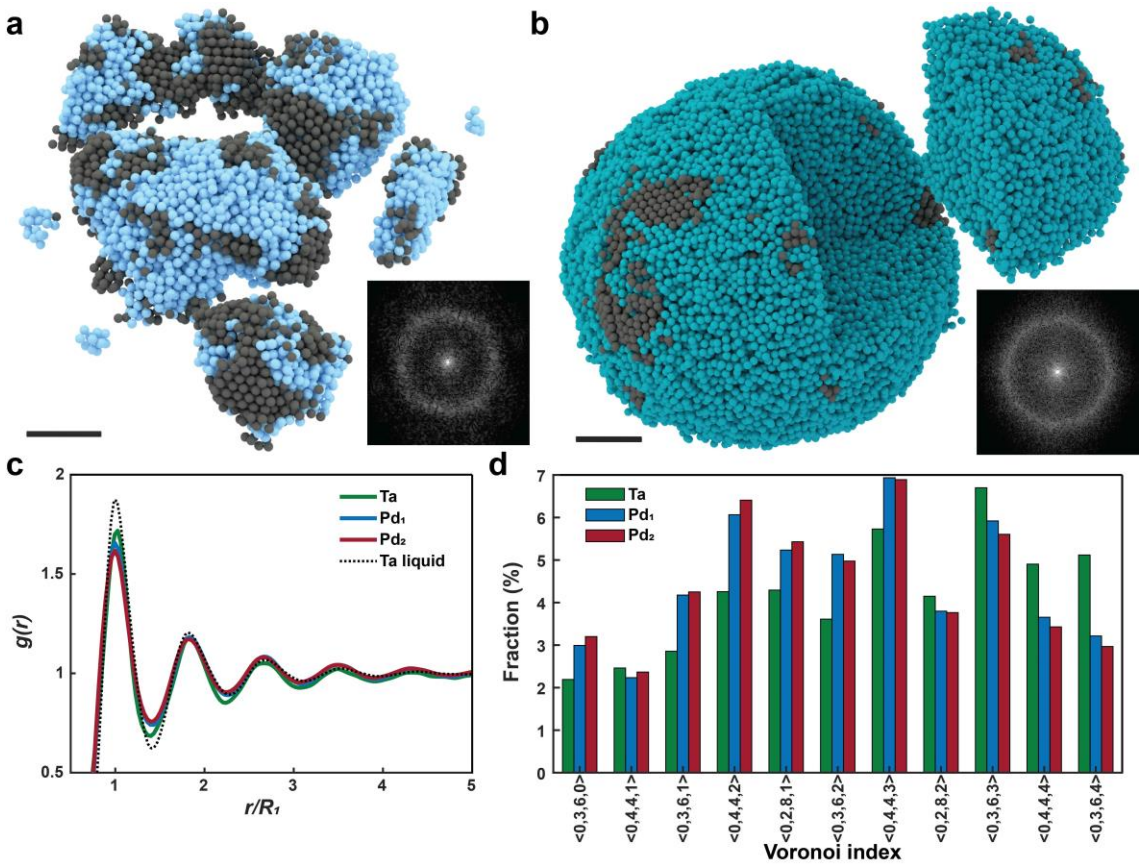

Fig. 1 | Determination of the 3D atomic structure of amorphous materials. Experimental 3D atomic model of an amorphous Ta film (**a**) and Pd nanoparticle (Pd_1) (**b**) with surface crystal nuclei in gray. Scale bar, 2 nm. The Fourier transform of the 0° experimental images of the materials shows the amorphous rings (insets). **c**, Radial distribution functions of the Ta film (green), two Pd nanoparticles (Pd_1 in blue and Pd_2 in red) and an MD simulated Ta liquid (dotted curve), showing the typical amorphous characteristics. **d**, 11 most populated Voronoi polyhedra in the three experimental materials, where the Voronoi index is arranged with the increase of the coordination number.

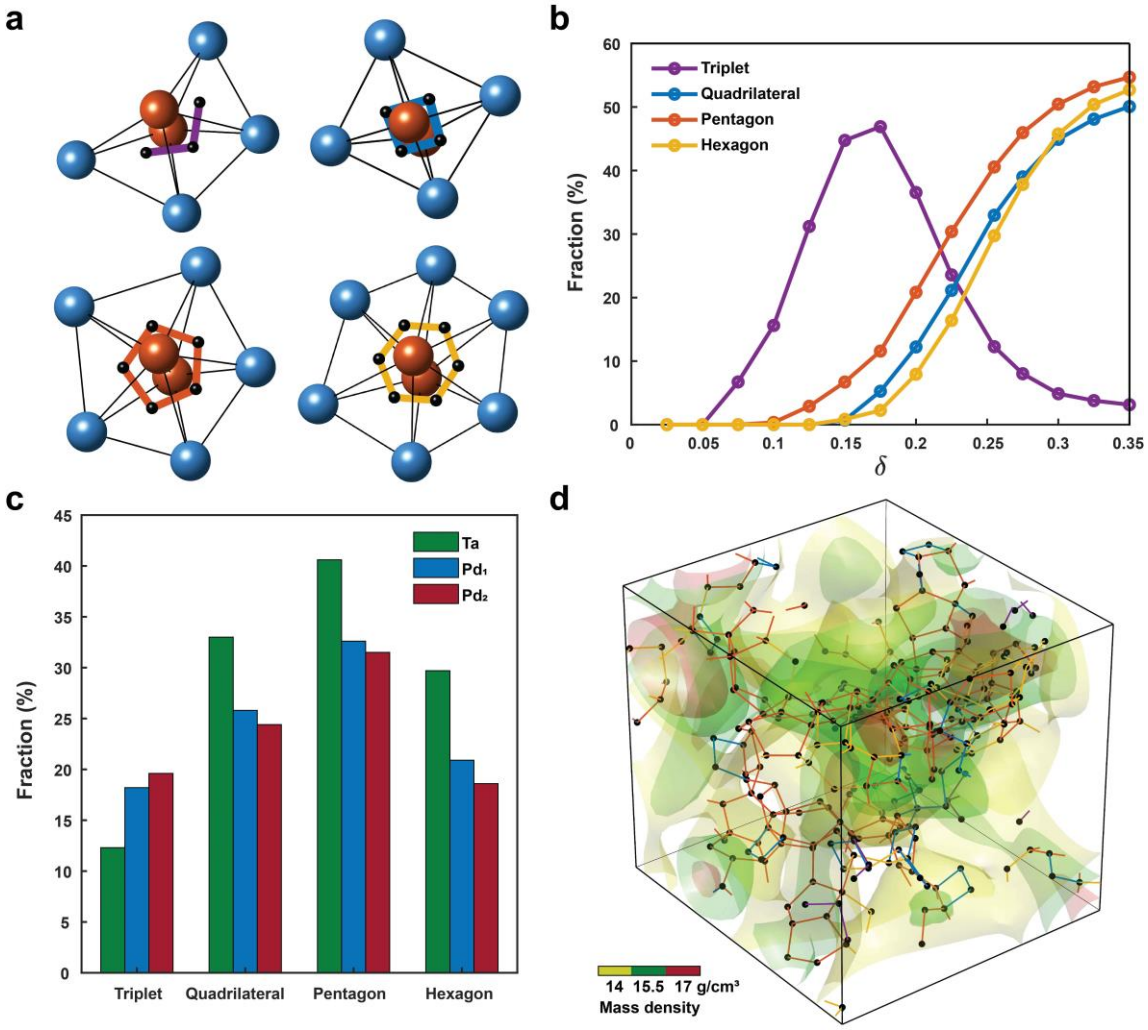

Fig. 2 | Polytetrahedral packing of amorphous Ta and Pd materials. a, Four most populated atomic motifs (triplets, quadrilateral, pentagonal and hexagonal bipyramids) in the amorphous Ta film, Pd_1 and Pd_2 nanoparticles, where the bond between two capping atoms (brown) is shared by all tetrahedra (black lines) with the surrounding atoms in blue. The four motifs are represented by a three- (purple), four- (blue), five- (orange) and six-fold skeleton (yellow), which connect the centroids (black dots) of the tetrahedra. **b**, Population of the four atomic motifs in the Ta film as a function of δ, where each value in the x-axis represents the maximum allowed δ in the tetrahedra forming the motifs. **c**, Distribution of the four atomic motifs in the amorphous Ta film (green), Pd_1 (blue) and Pd_2 (red) nanoparticles with δ = 0.255. **d**, Observation of the 3D local mass density heterogeneity caused by the packing of the four

motifs in the Ta film, where three-, four-, five- and six-fold skeletons are shown in purple, blue, orange and yellow, respectively.

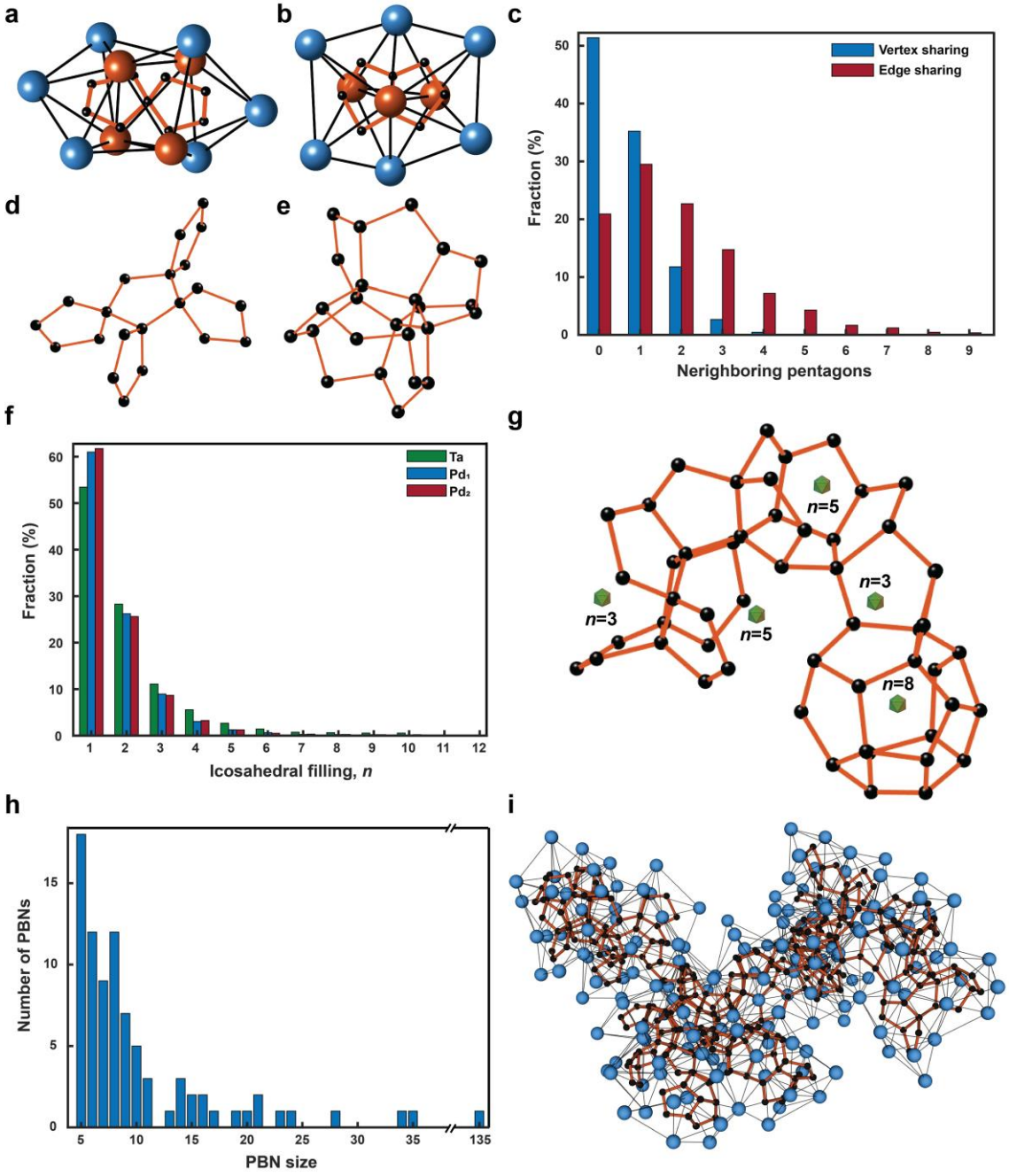

Fig. 3 | Direct observation of pentagonal bipyramid networks in monatomic amorphous materials. a, Vertex-sharing of two pentagonal bipyramids with different capping atoms (brown). **b**, Edge-sharing of two pentagonal bipyramids with a common capping atom (brown). **c**, Population of pentagonal bipyramids as a function of the number of vertex- and edge-sharing neighbours in the amorphous Ta film. Pentagonal bipyramid clusters with the most vertex- (**d**)

and edge-sharing neighbours (**e**) in the three amorphous materials. **f**, Population of pentagonal bipyramids filling partial icosahedral sites (*n*). The formation of a full icosahedron requires *n* = 12. **g**, Five-fold skeleton of a representative PBN, containing 5 partial icosahedra with n = 3, 5, 5, 3 and 8. The center of each partial icosahedron is labelled by an icosahedron (green). **h**, Histogram of the PBNs as a function of their size (i.e. the number of pentagonal bipyramids) in the Ta thin film. **i**, The largest PBN in the amorphous materials, containing 135 pentagonal bipyramids formed by 165 Ta atoms (blue balls). The network of the five-fold skeletons is represented by black dots and orange lines with the Ta atoms in blue.

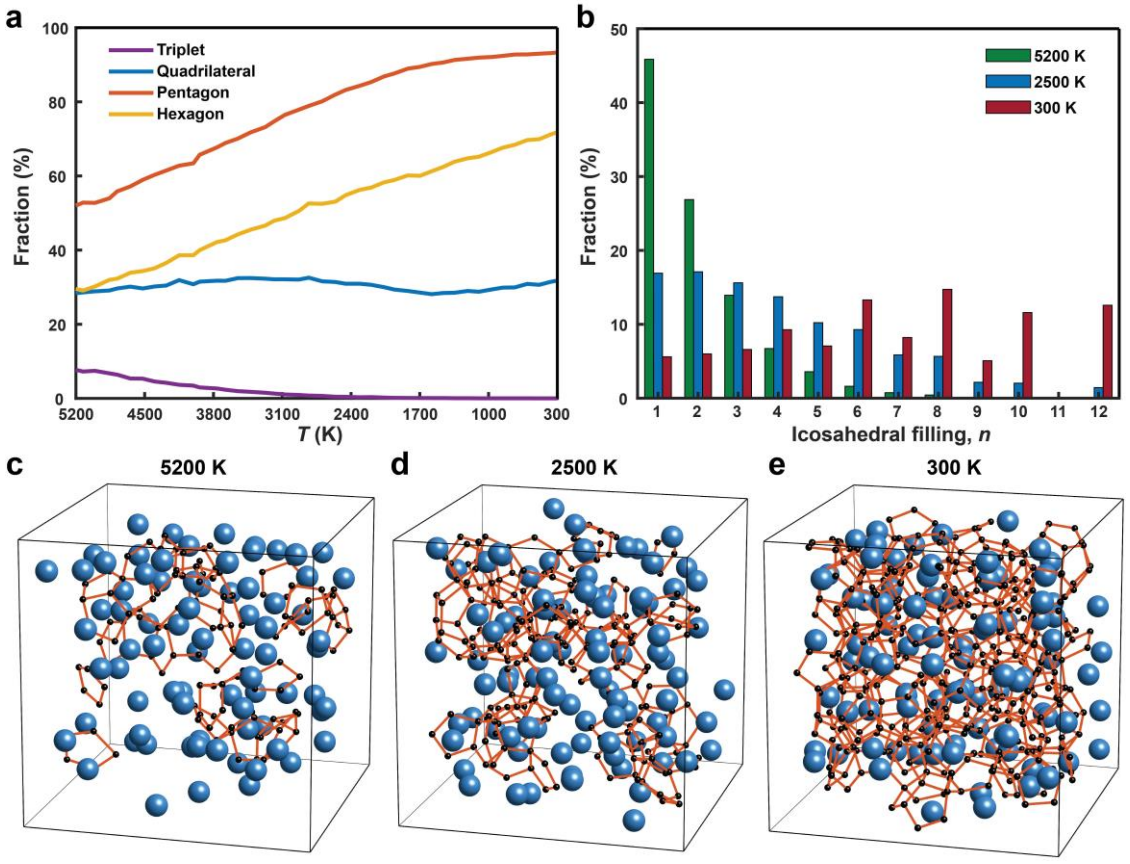

Fig. 4 | Observation of pentagonal bipyramids networks in an MD simulated Ta liquid and metallic glass. a, Population of the four most populated atomic motifs (triplets, quadrilateral, pentagonal and hexagonal bipyramids) as a function of the temperature. **b**, Population of pentagonal bipyramids filling partial icosahedral sites (*n*) at the liquid temperature (5200 K), during quench (2500 K) and at room temperature (300 K). **c**-**e**, Snapshot

of a fraction of the atomic models and PBNs at the above three temperatures. Ta atoms are shown as blue balls and the PBNs as orange lines and black dots. The PBNs quickly grow in size and a fraction of full icosahedra are formed with the decrease of the temperature.

METHODS

Physical vapor deposition of amorphous Ta thin films. Ta thin films were prepared in the ultrahigh vacuum system associated with the SPLEEM (spin polarized low energy electron microscope) instrument at the National Center for Electron Microscopy of the Molecular Foundry at Lawrence Berkeley National Laboratory. Prior to sample growth, Si_3N_4-window grids were cleaned by heating to about 700 K in ultrahigh vacuum. For film depositions, the grids were held in a liquid nitrogen cryostat, where tests using Pt1000 sensors indicated that the temperature of the grids remained in the range of 130 – 150 K during depositions. High-purity physical vapor beams were produced by heating small charges of Ta in a water-cooled electron beam evaporator and depositing on the Si_3N_4-windows to grow amorphous Ta films. The growth chamber has a base pressure in the 10^{-11} torr range, and during sample deposition pressure did not exceed the low 10^{-9} torr range. Growth rates were calibrated by growing test-films on single crystal Ru(0001), W(110) and Cu(100) substrates while observing low energy electron reflectivity oscillations associated monolayer-by-monolayer epitaxial growth, as well as by measuring peak height ratios in Auger electron spectra of the test samples. All samples were deposited using growth rates in the range of 0.2 – 1 atomic monolayer per minute (or about 2 – 10 nm/hour). After finishing deposition, all samples were coated with ~2 nm amorphous carbon deposited from another e-beam evaporator to protect the amorphous structure.

Synthesis of amorphous Pd nanoparticles. The amorphous Pd nanoparticles were synthesized by following a previously reported heating-up method with a minor modification[31,32]. Typically, 407 mg palladium (II) acetylacetonate, 4 mL trioctylphosphine and 40 mL oleylamine were placed into a round-neck flask. The mixture was degassed at room temperature for 1 hour under vacuum. The reaction solution was then slowly heated to 280 °C (c.a. 3 ºC/min) under nitrogen, and kept at 280ºC for 30 min. The reaction was quenched by removing the heating mantle and blowing cool air. The product was purified through centrifugation after precipitation with ethanol and the resulting Pd nanoparticles were redispersed in toluene. The procedure of ligand exchanges with NH_2^- was as follows[33]: 20 mg of $NaNH_2$ was dissolved in 10 mL dimethyl sulfoxide (DMSO), followed by an addition of 10 mL of the Pd nanoparticle toluene solution (0.4 mg/mL). The mixture was stirred for two days to complete the ligand exchange. The product was collected by centrifugation and washed by acetone one more time. The purified product was obtained by centrifugation and dispersed in nanopore water. Acetone, toluene, DMSO, oleylamine (70%), palladium (II) acetylacetonate (98%), sodium amide ($NaNH_2$, 95%), and trioctylphosphine (97%) were obtained from Sigma Aldrich.

ADF-STEM data acquisition. Tomographic tilt series of Ta thin films and Pd nanoparticles were acquired using the TEAM I microscope at the National Center for Electron Microscopy. The microscope was operated in annular dark field mode with electron energy of 300 keV (Extended Data Table 1). At each tilt angle, three sequential images were taken with a dwell time of 3 μs to minimize the dose rate and drift distortion in each image. To mitigate the beam damage to the samples, the total electron dose of each tilt series was optimized to be about 8-

10×10^5 $e^-/Å^2$ (Extended Data Table 1). Images taken at 0º tilt angle before, during and after the tilt series indicate that a minimal structural change of the samples throughout the experiment (Extended Data Fig. 3a-g).

Image pre-processing. The following four steps were used to perform image pre-processing.

i) Drift correction[34]. To correct sample drift, three ADF-STEM images at each tilt angle were registered using the following procedure. First, a region of 400 × 400 pixels from the second and third images was cropped and scanned over the first one with a step size of 0.05 pixel. Next, the cross-correlation coefficient between images was calculated, where the relative drift vectors were identified by the maximum cross-correlation. The ADF-STEM images have a typical drift of less than 1 pixel. We then applied drift distortion correction to each image along the slow scan direction. By assuming a linear drift during the data acquisition, the drift for each pixel in the image can be determined and corrected by interpolating the raw image with drift corrected pixel positions. Finally, the three drift corrected images at each tilt angle were averaged for denoising.

ii) Image denoising. The experimental images have both Poisson and Gaussian noise. A general algorithm named Block-matching and 3D filtering (BM3D)[35] has been proven effective in previous AET experiments[25,34,36], and was applied to denoise the drift corrected images. To optimize the BM3D parameters, we first estimated the Gaussian and Poisson noise in the experimental images, and then applied BM3D to denoise a simulated ADF-STEM image with the same noise level by varying denoising parameters. The best parameters were identified by maximizing the cross-correlation between the denoised image and the simulated noise-free image. These optimized parameters were used to denoise all the experimental images.

iii) Background subtraction. For each denoised image, a mask slightly larger than the sample was generated by thresholding. From the background outside the mask, the background level within the mask was estimated using Laplacian interpolation. The estimated background was subtracted from the denoised image.

iv) Image alignment. The images in each tilt series were aligned using the following procedure. The tilt series of the two Pd nanoparticles was aligned by the center of mass and common line method, as described in previous AET experiments[23,24]. For the Ta thin film, we first performed a pre-alignment by using cross-correlation between the images of neighbouring tilt angles. Next, we chose an isolated region in the thin film and used the common line method and the center of mass[23,24] to align it along the tilt axis and perpendicular to the tilt axis, respectively. We repeated this alignment process until no further improvement could be made.

3D reconstruction with RESIRE. After image pre-processing, each experimental tilt series was computed by the Real Space Iterative Reconstruction (RESIRE) algorithm[22]. The algorithm minimizes the difference between the experimental and computed images using the gradient descent method. The error function and the gradient are defined as,

$$\varepsilon_\theta(O) = \frac{1}{2}\sum_{x,y}|\Pi_\theta(O)\{x,y\} - b_\theta\{x,y\}|^2 \qquad (1)$$

$$\nabla\varepsilon_\theta(O)\{u,v,w\} = \Pi_\theta(O)\{x,y\} - b_\theta\{x,y\} \quad where \begin{bmatrix}u\\v\\w\end{bmatrix} = R_\theta\begin{bmatrix}x\\y\\z\end{bmatrix} \quad for\ some\ z \qquad (2)$$

where ε_θ is the error function of a 3D object O at tilt angle θ, $\Pi_\theta(O)$ calculates the projection of the object O at angle θ, b_θ is the experimental image at angle θ, $\{x,y,z\}$ are the coordinates, ∇ is the gradient, R_θ is the rotation matrix transforming coordinates $\{x,y,z\}$ to $\{u,v,w\}$. More mathematical description of RESIRE and its superior performance to other algorithms, such as the generalized Fourier iterative reconstruction and the simultaneous iterations reconstruction technique, will be presented in a follow-up paper.

The two Pd nanoparticles were directly reconstructed by RESIRE. For the Ta thin film, we first performed a large volume reconstruction with RESIRE. After estimating the thickness variation of the Ta thin film, we applied scanning AET to do multiple local volume reconstructions and then patched them together to obtain a full reconstruction[37]. Previous study has shown that scanning AET can improve the reconstruction of 2D layered and thin film samples over AET[37].

From the 3D reconstructions of the Pd nanoparticles and Ta film, we performed angular refinement and image alignment until the results converged. Next, we traced and refined the 3D atomic coordinates from each reconstruction (see the section below), from which reference images were calculated at the corresponding tilt angles. The experimental tilt angles and images were further refined and re-aligned using these reference images. After these procedures, the final reconstructions were performed for all three samples.

Determination and refinement of 3D atomic coordinates. From the reconstructions of the Pd nanoparticles and the Ta thin film, we determined their 3D atomic coordinates using the following steps.

i) We interpolated each reconstruction onto a finer grid with three times oversampling using the spline method. All the local maxima in the reconstruction were identified and the positions of potential atoms were extracted from a local volume of 0.8 Å × 0.8 Å × 0.8 Å with a polynomial fitting method[25,38]. For every potential atom, a minimum distance of 2 Å to its neighbouring atoms have to be satisfied. This constraint is based on the fact that all the interatomic distances in our samples are larger than 2 Å. After iterating through all local maxima, a list of potential atoms was obtained.

ii) To separate non-atoms from the potential atoms, we employed the K-mean clustering method[25,36,39] based on the integrated intensity of a local volume (0.8 Å × 0.8 Å × 0.8 Å) around each potential atom position. After excluding non-atoms, the potential atomic models of the two Pd nanoparticles and Ta film were obtained.

iii) By carefully comparing the individual atomic positions in the potential atomic models with the 3D reconstructions, we manually corrected a small fraction of unidentified or misidentified atoms.

iv) We repeated step ii) and iii) until no further improvement could be made, resulting in the 3D atomic models of the three amorphous materials.

v) The 3D atomic coordinates in each model were refined by minimizing the error between the experimental and computed images using gradient descent as described elsewhere[22,25,34,36]. The refinement results are shown in Extended Data Table 1.

3D precision estimation. To estimate the 3D precision of our method, we performed multislice simulations[40,41] to calculate ADF-STEM images from the Ta atomic model using the same experimental parameters specified in Extended Data Table 1. A tilt series of 46 multislice images was computed at the experimental tilt angles. To account for the electron probe size and other effect, the image was convolved with a Gaussian function. A representative multislice ADF-STEM image at 0° tilt angle is shown in Extended Data Fig. 3i, which is in good agreement with the corresponding experimental image (Extended Data Fig. 3h). From the 46 multislice ADF-STEM images, we used the same reconstruction, tracing and refinement procedure to obtain a new 3D atomic model. By comparing the new atomic model with the experimental one, we found 98.1% of the atoms are identical with a root-mean-square deviation of 18 pm (Extended Data Fig. 3j).

The radial distribution function. We used the following procedure to calculate the radial distribution function (RDF) of each sample. i) We computed the histogram of atom pair distances in spherical shells with a shell thickness of 0.1 Å. ii) The counts in each spherical shell were divided by the volume of the spherical shell, yielding

the density of atom pairs as a function of the pair distance. iii) The RDF was scaled to approach one at large pair distances. Using this procedure, we calculated the RDFs of all the atoms in the Ta thin film and two Pd nanoparticles. From the RDF of each material, we determined the first valley position, corresponding to the first nearest neighbour shell distance. This distance was used to compute the local bond orientational order parameter (see the section below), from which crystal nuclei were identified. After excluding the crystal nuclei, the RDFs of the disordered atoms in the amorphous materials were re-calculated, shown in Fig. 1c.

The local bond orientational order parameter. We calculated the averaged local bond orientational order parameters (Q_4 and Q_6) to quantify the disorder of the amorphous materials[26,42]. The Q_4 and Q_6 values were computed based on the procedure published elsewhere[42], where the first nearest neighbour shell distance (Fig. 1c) was used as a constraint. Q_4 and Q_6 were used to calculate the normalized bond orientational order parameter, defined as $\sqrt{{Q_4}^2 + {Q_6}^2}/\sqrt{Q_{4\,\mathrm{fcc}}^2 + Q_{6\,\mathrm{fcc}}^2}$, where $Q_{4\,\mathrm{fcc}}$ and $Q_{6\,\mathrm{fcc}}$ are the refence values of the fcc lattice. We separated crystal nuclei from amorphous structure by setting the normalized bond order parameter larger than or equal to 0.5 (red dashed lines in Extended Data Fig. 4c-e)[22].

Voronoi tessellation and local mass density distribution. The Voronoi tessellation of each 3D atomic model was calculated by following procedure published elsewhere[4]. To characterize the nearest neighbour atoms around each center atom, a regulation was applied to each Voronoi polyhedron, where neighbouring atoms with the facet area less than 1% of the total Voronoi surface area or outside the first nearest neighbour shell were removed during the analysis[43]. All the Voronoi polyhedra were then indexed by $\langle n_3, n_4, n_5, n_6 \rangle$ with n_i denoting the number of *i*-edge faces. The coordination number was calculated by $\sum_i n_i$.

The mass density for each atom was calculated by dividing the atomic mass by its atomic volume, which is defined as the volume of its Voronoi polyhedron without regulation. The densities at all atomic positions were interpolated onto a 3D grid and then convolved with a Gaussian kernel. The width of the Gaussian kernel was set as the first nearest neighbour shell distance defined by the RDF. Using this procedure, we obtained the local mass density distribution of the three amorphous materials (Extended Data Fig. 5).

Polytetrahedral packing analysis. To identify all the tetrahedra in each amorphous material, we used the distortion parameter (δ) defined in the main text, where the maximum edge length of each tetrahedron cannot be larger than the first nearest neighbour shell distance (Fig. 1c). The population of the tetrahedra strongly depends on δ. With $\delta > 0.2$, more than 96.8% of the atoms in the three amorphous materials form tetrahedra (green curves in Extended Data Fig. 4g-i). From these tetrahedra, we searched for polytetrahedral motifs and found four main motifs (Fig. 2a): i) triplets with three face-sharing tetrahedra (but the 1st and 3rd tetrahedron do not share a face); ii) quadrilateral bipyramids with four face-sharing tetrahedra; iii) pentagonal bipyramids with five face-sharing tetrahedra; and iv) hexagonal bipyramids with six face-sharing tetrahedra. All these four polytetrahedral motifs share two capping atoms (brown atoms in Fig. 2a). Although we observed other motifs in the amorphous materials, their population is much smaller than the four main motifs. We represented the four main motifs by three-, four-, five- and six-fold skeletons, which connect the centroids of the tetrahedra (Fig. 2a). The fraction of four main motifs, defined as the number of tetrahedra in each motif divided by the total number of tetrahedra in each amorphous material, strongly depends on δ (Extended Data Fig. 4g-i). The sum of the fraction of four main motifs can be larger than 1 because some tetrahedra are overlapped among different motifs. By choosing $\delta = 0.255$[13,28],

we found the polytetrahedral packing of the four motifs is strongly correlated with the local mass density heterogeneity (Extended Data Fig. 5).

Pentagonal bipyramid networks. We searched for the PBNs in each amorphous material using the following procedure. i) From the polytetrahedral packing of the sample, we only kept pentagonal bipyramids, which are represented by five-fold skeletons. ii) We started a PBN by choosing a five-fold skeleton and identifying all its edge-sharing skeletons. iii) We repeated step ii) until all the edge-sharing skeletons in the PBN were found. iv) We started a new PBN and repeated the procedure. v) After identifying all the PBNs in the sample, we only kept those PBNs with five or more pentagonal bipyramids. The five largest PBNs in the Ta thin film, two Pd nanoparticles and MD simulated Ta liquid (5200K) are shown in Extended Data Figs. 8 and 9b-f. The PBN size is defined as the number of pentagonal bipyramids in the network (Extended Data Fig. 7d-f). The PBN length was measured along the longest direction of the network (Extended Data Fig. 7g-i). We used the same procedure to find the quadrilateral and hexagonal bipyramid networks in each amorphous material.

Molecular dynamics simulations. To understand our experimental observations, we performed molecular dynamics simulations of a Ta bulk system using the LAMMPS package[44]. The system consisted of 31250 atoms using the embedded-atom-method interatomic potential[14] with periodic boundary conditions. The system was melted and equilibrated at 5200 K before quenching the system at a cooling rate of 10^{13} K/s using the isothermal-isobaric ensemble. The polytetrahedral packing analysis was performed on atomic configurations throughout the quench process and we observed similarities between the experimental amorphous materials and the MD simulations of liquids. This realistic interatomic potential was chosen for three reasons. First, the interatomic potential was developed with a focus on the metallic glass and liquid phases. Second, the simulated metallic glass structure factors correlate well with the experimental data[14]. Third, the simulated liquid phase RDF has the lowest least-square fitting error to the experimental Ta RDF (Fig. 1c) compared to other potentials[45,46], although all these interatomic potentials show similar PBNs and trends through the glass transition.

31. Liu, Y., Wang, C., Wei, Y., Zhu, L., Li, D., Jiang, J. S., Markovic, N. M., Stamenkovic, V. R. & Sun, S. Surfactant-Induced Postsynthetic Modulation of Pd Nanoparticle Crystallinity. *Nano Lett.* **11**, 1614–1617 (2011).
32. Kim, S.-W., Park, J., Jang, Y., Chung, Y., Hwang, S., Hyeon, T. & Kim, Y. W. Synthesis of Monodisperse Palladium Nanoparticles. *Nano Lett.* **3**, 1289–1291 (2003).
33. Nag, A., Kovalenko, M. V., Lee, J.-S., Liu, W., Spokoyny, B. & Talapin, D. V. Metal-free Inorganic Ligands for Colloidal Nanocrystals: S^{2-} , HS^{-} , Se^{2-} , HSe^{-} , Te^{2-} , HTe^{-} , TeS_3^{2-} , OH^{-} , and NH_2^{-} as Surface Ligands. *J. Am. Chem. Soc.* **133**, 10612–10620 (2011).
34. Xu, R., Chen, C.-C., Wu, L., Scott, M. C., Theis, W., Ophus, C., Bartels, M., Yang, Y., Ramezani-Dakhel, H., Sawaya, M. R., Heinz, H., Marks, L. D., Ercius, P. & Miao, J. Three-dimensional coordinates of individual atoms in materials revealed by electron tomography. *Nat. Mater.* **14**, 23 (2015).
35. Dabov, K., Foi, A., Katkovnik, V. & Egiazarian, K. Image Denoising by Sparse 3-D Transform-Domain Collaborative Filtering. *IEEE Trans. Image Process.* **16**, 2080–2095 (2007).
36. Yang, Y. *et al*. Deciphering chemical order/disorder and material properties at the single-atom level. *Nature*. **542**, 75–79 (2017).

37. Tian, X. *et al.* Correlating the three-dimensional atomic defects and electronic properties of two-dimensional transition metal dichalcogenides. *Nat. Mater.* (2020). https://doi.org/10.1038/s41563-020-0636-5
38. Rogers, S. S., Waigh, T. A., Zhao, X. & Lu, J. R. Precise particle tracking against a complicated background: polynomial ftting with Gaussian weight. *Phys. Biol*. **4**, 220–227 (2007).
39. Lloyd, S. Least squares quantization in PCM. *IEEE Trans. Inf. Theory*. **28**, 129–137 (1982).
40. Ophus, C. A Fast Image Simulation Algorithm for Scanning Transmission Electron Microscopy. *Adv. Struct. Chem. Imaging*, 1–11 (2017).
41. Pryor, A., Ophus, C. & Miao, J. A streaming multi-GPU implementation of image simulation algorithms for scanning transmission electron microscopy. *Adv. Struct. Chem. Imaging*. **3**, 15 (2017).
42. Lechner, W. & Dellago, C. Accurate determination of crystal structures based on averaged local bond order parameters. *J. Chem. Phys.* **129** (2008).
43. Sheng, H. W., Luo, W. K., Alamgir, F. M., Bai, J. M. & Ma, E. Atomic packing and short-to-medium-range order in metallic glasses. *Nature* **439**, 419-425 (2006).
44. Plimpton, S. Fast Parallel Algorithms for Short-Range Molecular Dynamics. *J. Comput. Phys.* **117**, 1–19 (1995).
45. Ravelo, R., Germann, T. C., Guerrero, O., An, Q. & Holian, B. L. Shock-induced plasticity in tantalum single crystals: Interatomic potentials and large-scale molecular-dynamics simulations. *Phys Rev B*. **88**, 134101 (2013).
46. Purja Pun, G. P., Darling, K. A., Kecskes, L. J. & Mishin, Y. Angular-dependent interatomic potential for the Cu–Ta system and its application to structural stability of nano-crystalline alloys. Acta Mater. 100, 377–391 (2015).

Extended Data Table 1 | AET data collection, processing, reconstruction, refinement and statistics

	Ta film	Pd_1 nanoparticle	Pd_2 nanoparticle
Data Collection and Processing			
Voltage (kV)	300	300	300
Convergence semi-angle (mrad)	17.1	17.1	17.1
Probe size (Å)	0.7	0.7	0.7
Detector inner angle (mrad)	30	30	30
Detector outer angle (mrad)	195	195	195
Depth of focus (nm)	14	14	14
Pixel size (Å)	0.322	0.454	0.454
Number of projections	46	52	54
Tilt range (º)	-63.4	-72.0	-72.4
	+55.5	+66.4	+69.4
Electron dose (10^5 e/Å^2)	8.2	9.3	9.6
Reconstruction			
Algorithm	RESIRE	RESIRE	RESIRE
Oversampling ratio	3	4	3.5
Number of iterations	500	200	200
Refinement			
R_1 (%)[a]	15.5	8.5	6.9
R (%)[b]	14.2	5.2	4.5
B' factors (Å^2)	22.1	45.2	58.3
Number of atoms	8284	52308	76238
MDB ID			

[a]The R_1-factor is defined by Eq. (5) in ref. 36.

[b]The R-factor is defined by $R = \frac{1}{n}\sum_\theta \frac{\sum_{x,y}|\Pi_\theta(O)\{x,y\} - b_\theta\{x,y\}|}{\sum_{x,y}|b_\theta\{x,y\}|}$, where n is the number of projection images.

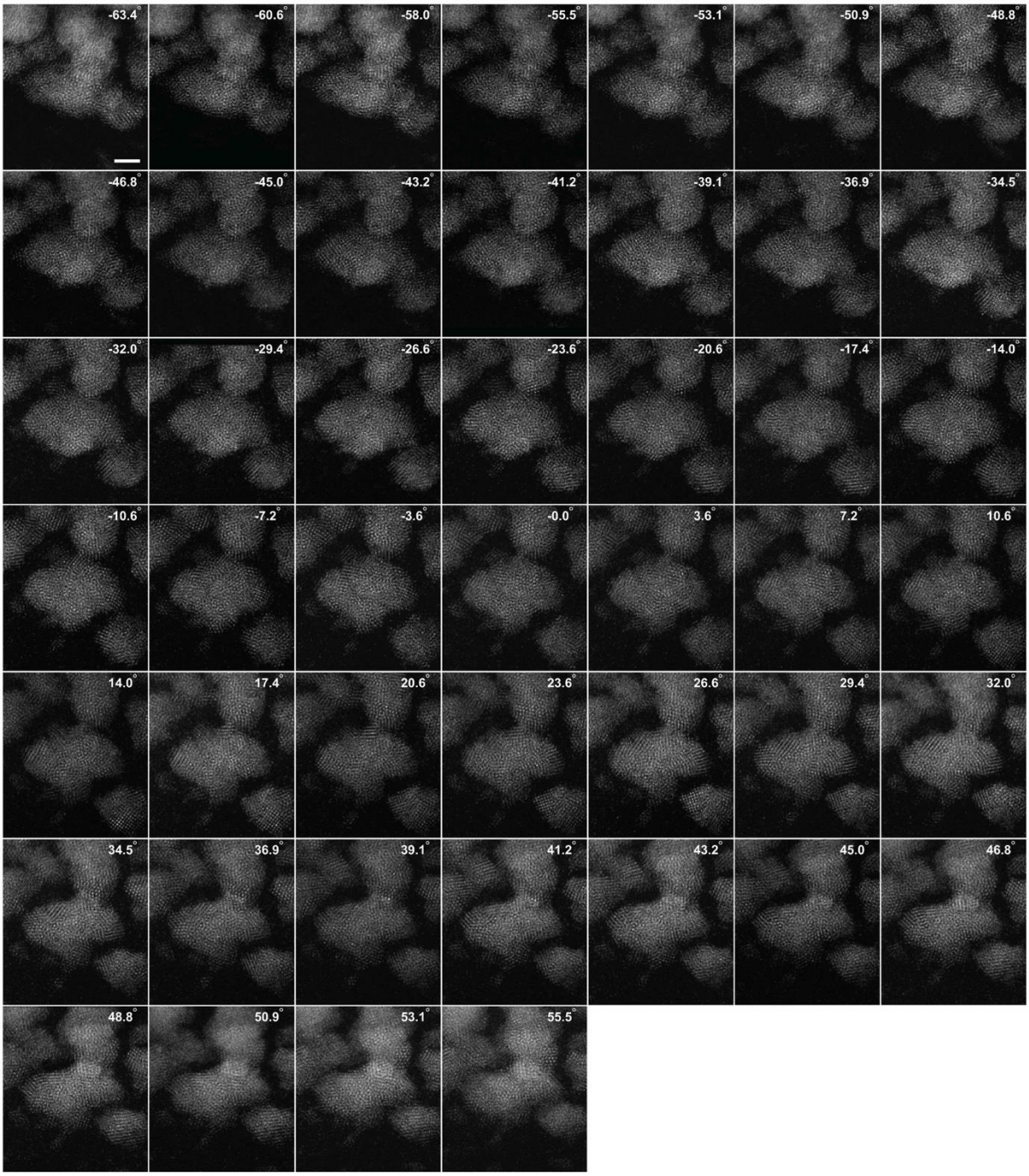

Extended Data Fig. 1 | Tomographic tilt series of an amorphous Ta thin film. 46 ADF-STEM images of the Ta film with a tilt range from −63.4° to +55.5°. The experimental parameters and the total electron dose are listed in table S1. Scale bar, 2 nm.

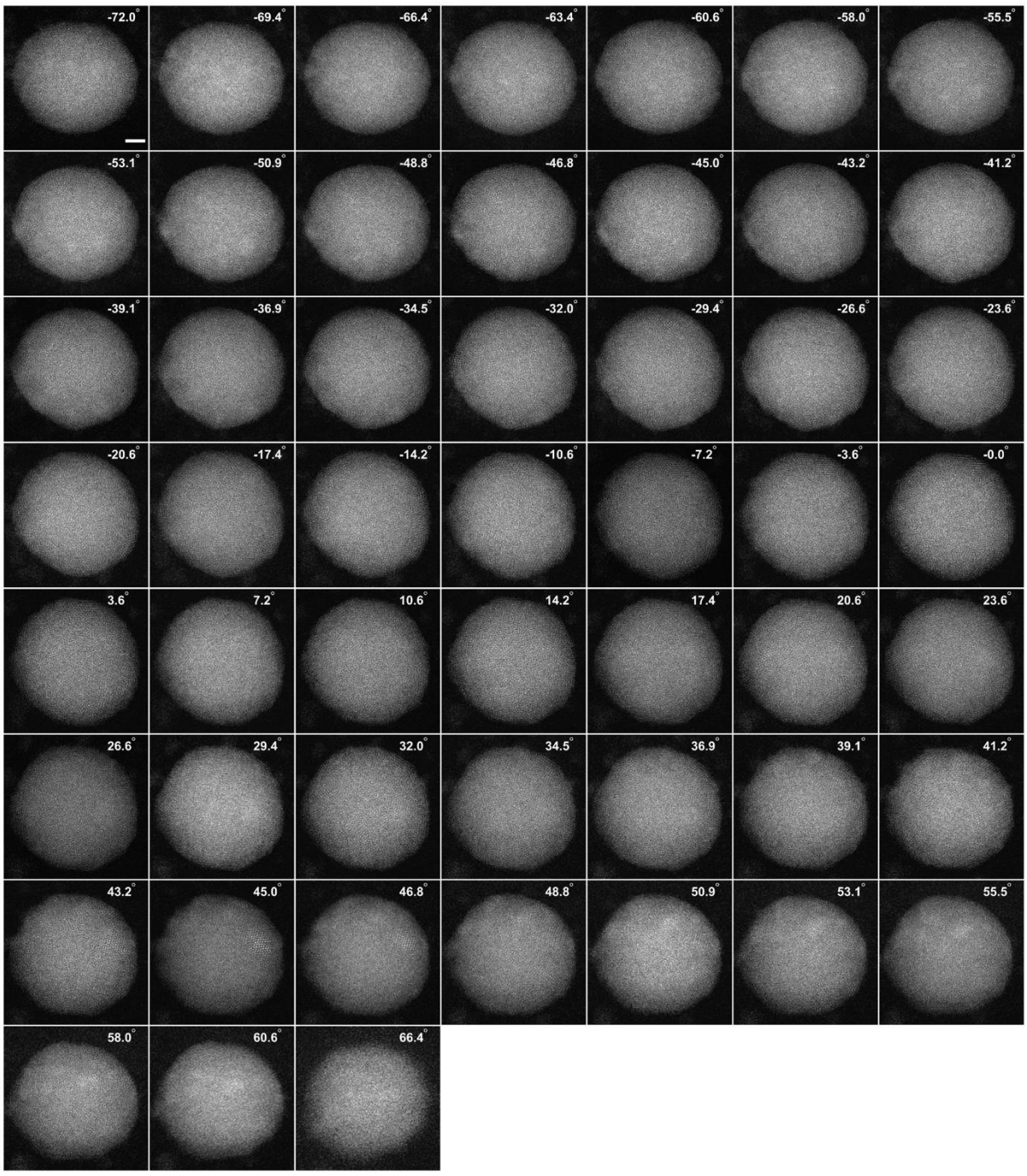

Extended Data Fig. 2 | Tomographic tilt series of an amorphous Pd nanoparticle (Pd_1). 52 ADF-STEM images of the Pd_1 nanoparticle with a tilt range from −72.0° to +66.4°. The experimental parameters and the total electron dose are listed in table S1. Scale bar, 2 nm.

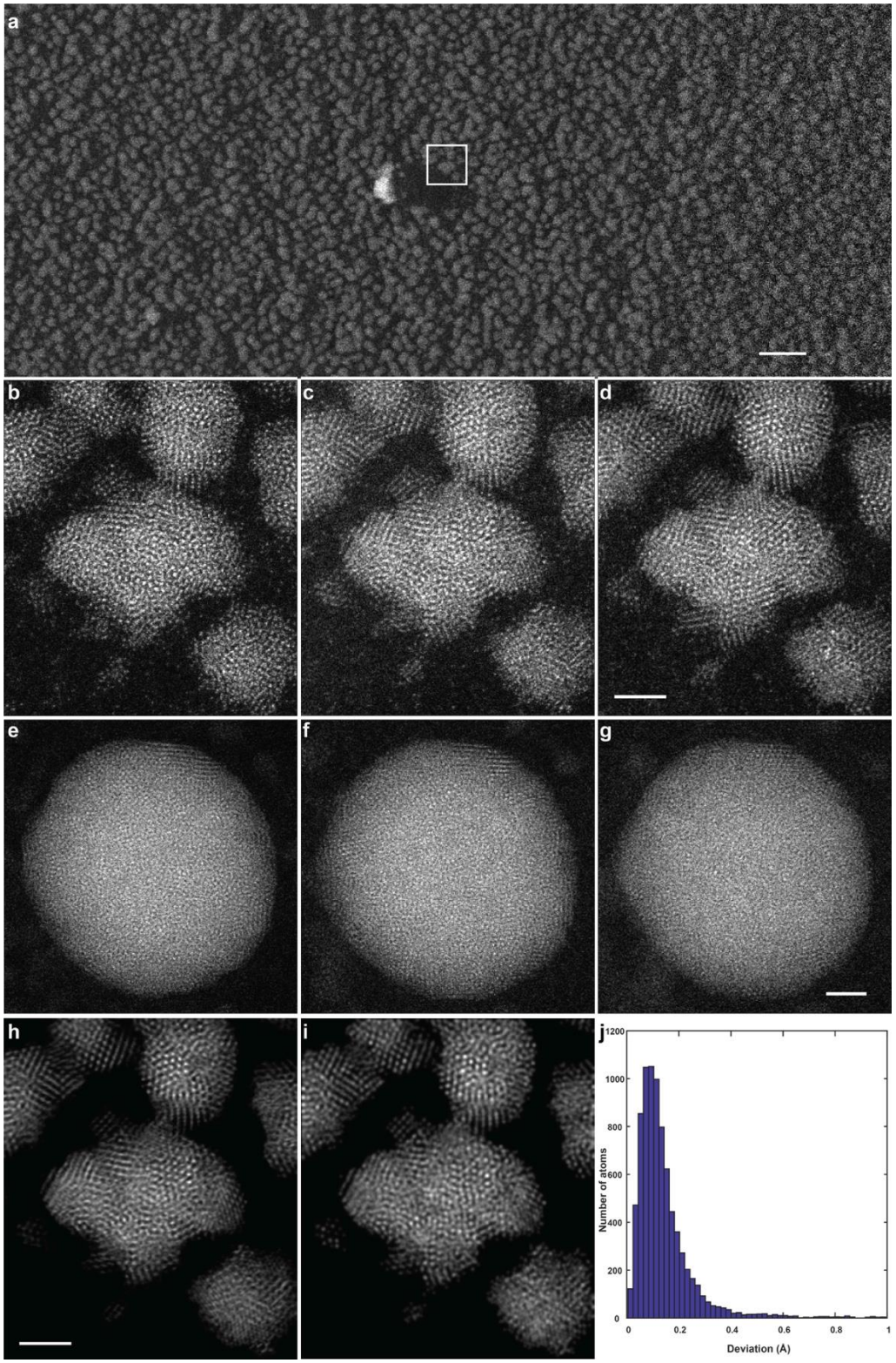

Extended Data Fig. 3 | Consistency check of the amorphous materials and 3D precision estimation of the experimental 3D atomic model. **a,** Low magnification overview of the Ta thin film. A tomographic tilt series was acquired from the region marked by the white square. ADF-STEM images taken before, during and after the experiment for the Ta thin film (**b-d**) and Pd_1 (**e-g**) nanoparticles, indicating a minimal change of the sample structure during the data acquisition. **h**, Experimental image of the amorphous Ta film after denoising. **i**, Multislice simulation image calculated from the experimental 3D atomic model of the Ta thin film. Using 46 multislice simulation images and the same reconstruction, atom tracing and refinement

procedure, we obtained a new 3D atomic model. **j**, Histogram of the root-mean-square deviation between the experimental 3D atomic model and the new 3D atomic model, showing 98.1% of the atoms are identical with a 3D precision of 18 pm. Scale bar, 20 nm in (**a**) and 2 nm in (**d, g, h**). All the images were taken at 0° tilt angle.

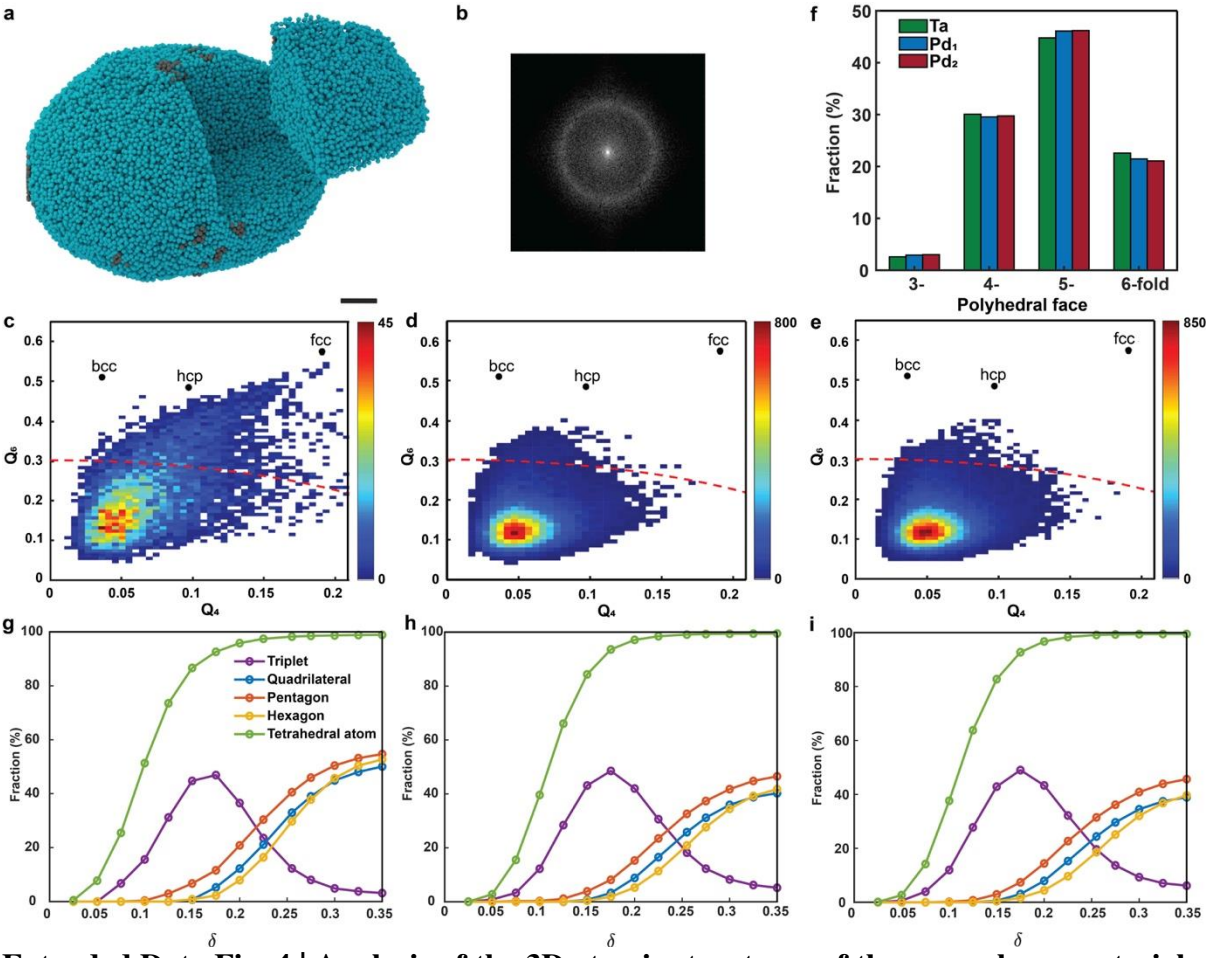

Extended Data Fig. 4 | Analysis of the 3D atomic structures of the amorphous materials. **a**, Experimental 3D atomic model of the Pd_2 nanoparticle with crystal nuclei in gray. Scale bar, 2 nm. **b**, The Fourier transform of the experimental image of the nanoparticle shows the amorphous rings. Averaged local bond orientational order parameters for the Ta film (**c**), Pd_1 (**d**) and Pd_2 (**e**) nanoparticles. Red dashed lines correspond to the normalized bond orientational order parameter equal to 0.5. **f**, The three-, four-, five- and six-edge face distribution for the Voronoi polyhedra in three samples, where the five-edge faces are the most abundant in all three samples. Fraction of the tetrahedral atoms and four polytetrahedral motifs (triplets, quadrilateral, pentagonal and hexagonal bipyramids) in the amorphous Ta film (**g**), Pd_1 (**h**) and Pd_2 (**i**) nanoparticles, as a function of δ, where each value in the x-axis represents the maximum allowed δ in the tetrahedra. The green curves show the fractions of the atoms in the three amorphous materials form tetrahedra. The purple, blue, orange and yellow curves show the fractions of four main motifs, defined as the number of tetrahedra in each motif divided by the total number of tetrahedra in each amorphous material.

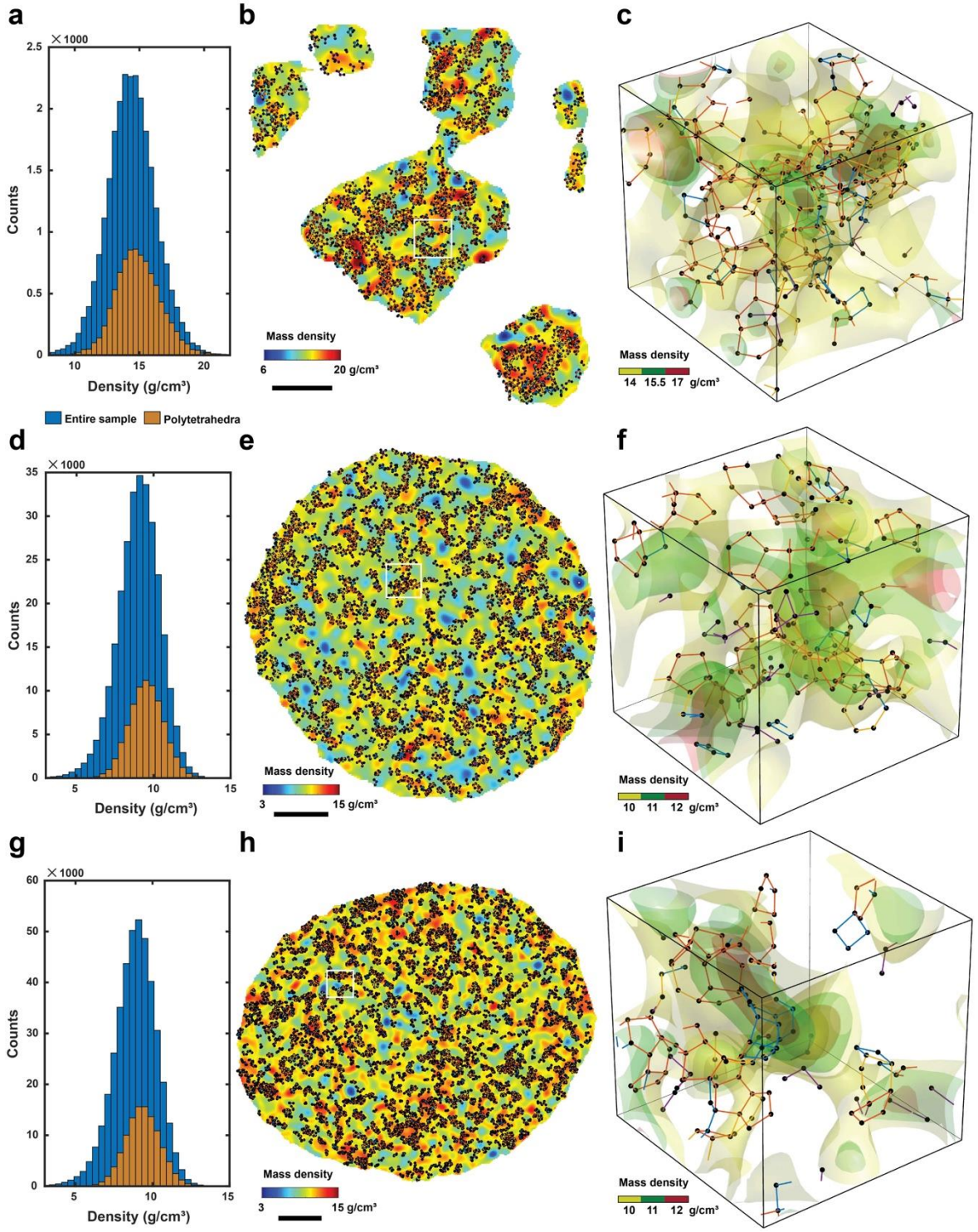

Extended Data Fig. 5 | Correlation of 3D local mass density heterogeneity and polytetrahedral packing. a, **d**, **g**, Mass density histograms of the polytetrahedral packing region (yellow) and the entire sample for the amorphous Ta film, Pd_1 and Pd_2 nanoparticles, respectively, where polytetrahedral packing shows higher averaged mass density. **b**, **e**, **h**, Observation of 3D local mass density heterogeneity in the Ta film, and Pd_1 and Pd_2 nanoparticles, respectively. A slice through each sample shows the local mass density heterogeneity (color) overlaid with three-, four-, five- and six-fold skeletons (black). **c**, **f**, **i**, 3D surface renderings of local mass density heterogeneity magnified from the square regions in (**b**), (**e**) and (**h**), respectively, which are overlaid with three- (purple), four- (blue), five- (orange) and six-fold (yellow) skeletons.

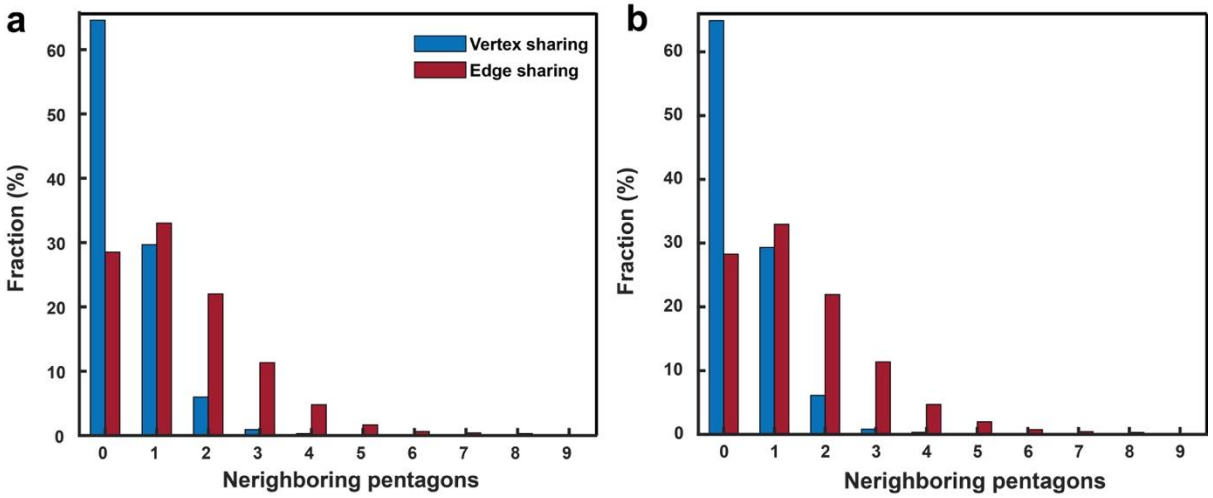

Extended Data Fig. 6 | Vertex- and edge-sharing the five-fold skeletons. Population of pentagonal bipyramids as a function of the number of vertex- (blue) and edge-sharing (red) neighbors in the amorphous Pd_1 (**a**) and Pd_2 (**b**) nanoparticles. Edge sharing of the five-fold skeletons have more neighbors than vertex-sharing of five-fold skeletons.

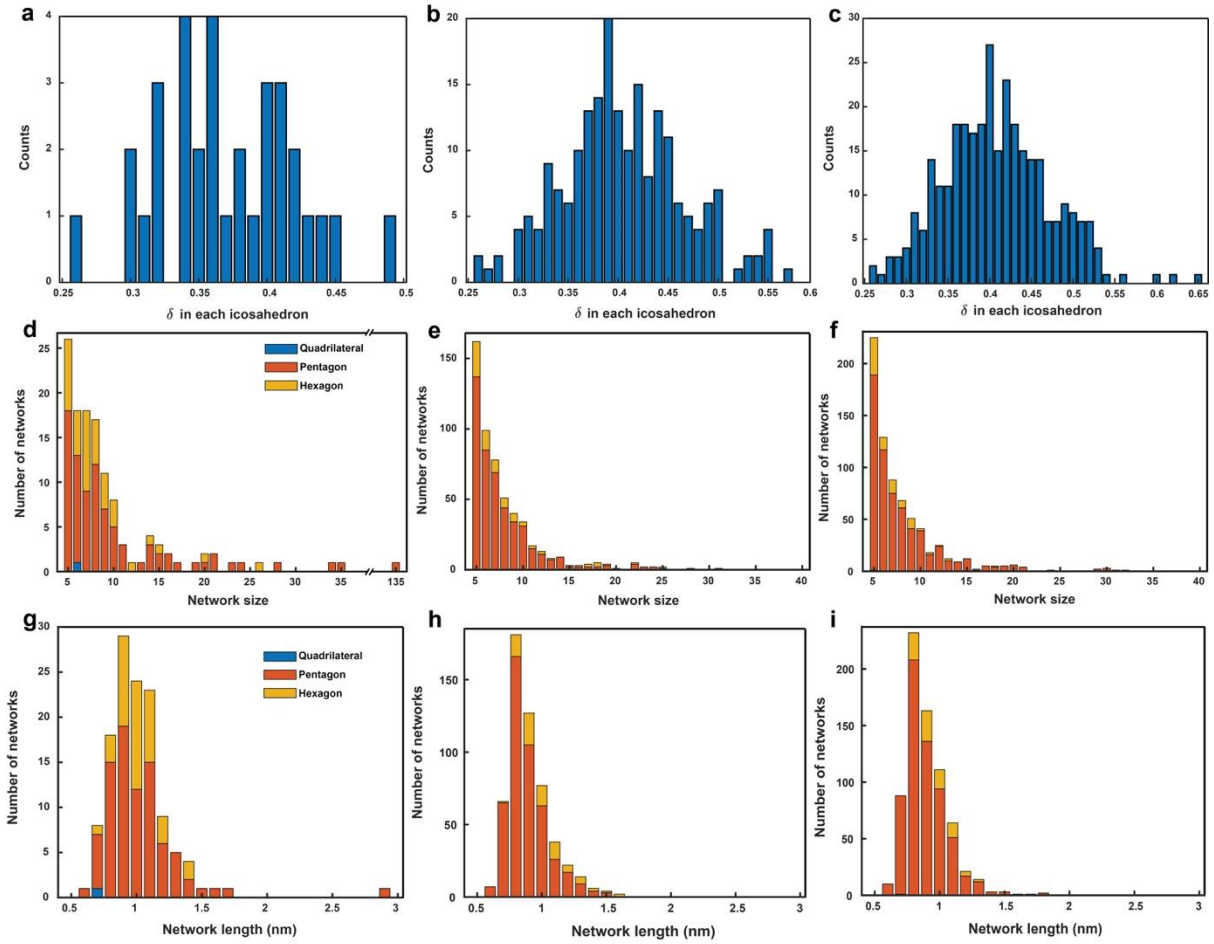

Extended Data Fig. 7 | Distortion of the icosahedra in the Voronoi tessellation and analysis of the quadrilateral, pentagonal, and hexagonal bipyramid networks. Number of icosahedra (counts) with <0,0,12,0> as a function the maximum δ in each icosahedron in the amorphous Ta film (**a**), Pd_1 (**b**) and Pd_2 (**c**) nanoparticles. Due to the large distortion parameter ($\delta > 0.255$), none of them were identified as icosahedra in our polytetrahedral packing analysis. Population of the quadrilateral (blue), pentagonal (orange), and hexagonal bipyramid (yellow) networks as a function of their size in the amorphous Ta thin film (**d**), Pd_1 (**e**) and Pd_2 (**f**) nanoparticles, where the network size is defined as the number of quadrilateral, pentagonal, and hexagonal bipyramids in the corresponding networks. Population of the quadrilateral (blue), pentagonal (orange), and hexagonal bipyramid (yellow) networks as a function of their length in the amorphous Ta thin film (**g**), Pd_1 (**h**) and Pd_2 (**i**) nanoparticles, where the network length is defined as the distance along the longest direction of each network.

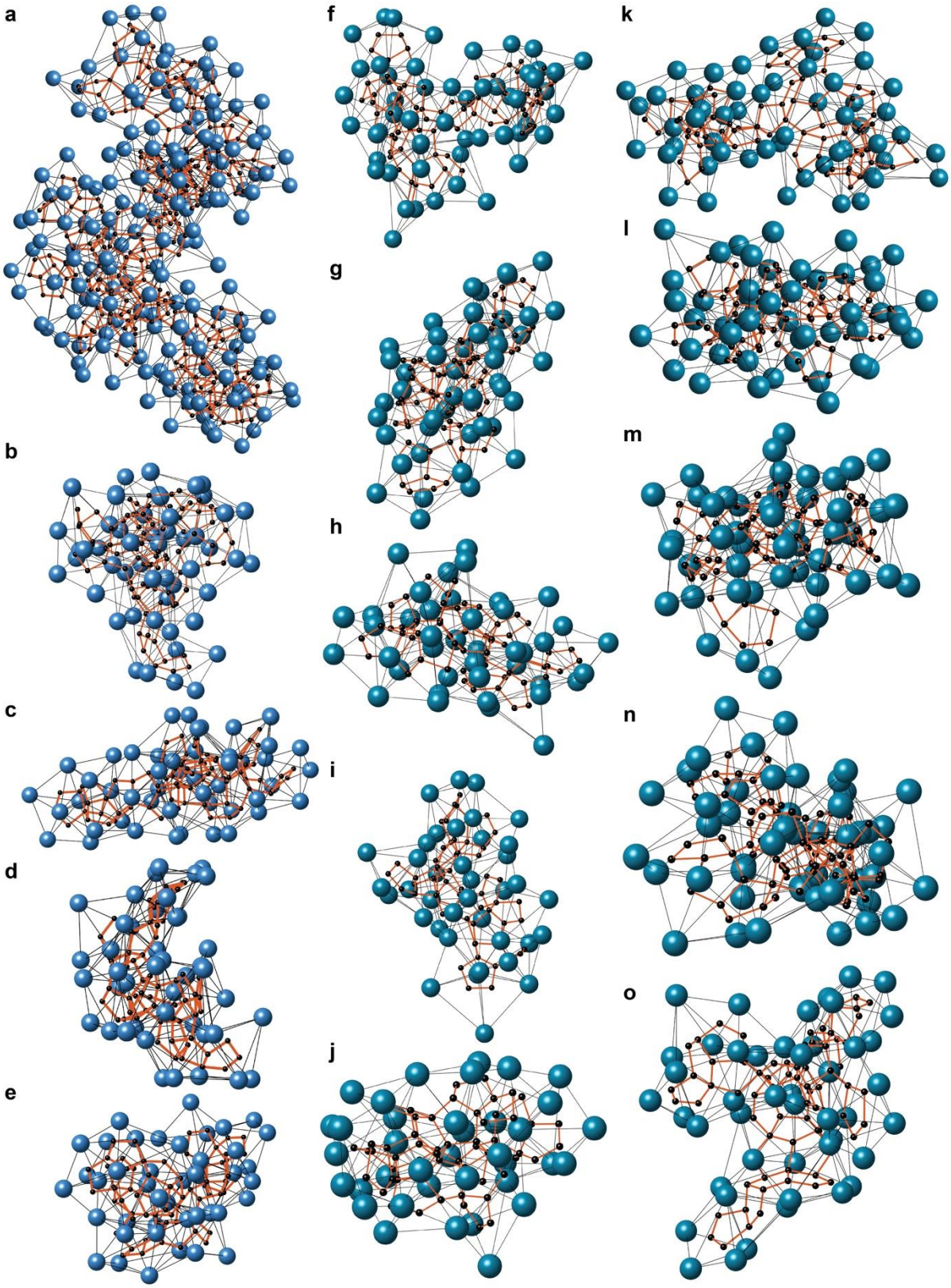

Extended Data Fig. 8 | Five largest PBNs the amorphous materials. a-e, Five largest PBNs in the amorphous Ta thin film with 135, 35, 34, 28 and 24 pentagonal bipyramids, respectively. **f-j**, Five largest PBNs in the amorphous Pd_1 nanoparticle with 31, 28, 25, 24 and 24 pentagonal bipyramids, respectively. **k-o**, Five largest PBNs in the amorphous Pd_2 nanoparticle with 32, 31, 30, 30 and 29 pentagonal bipyramids, respectively.

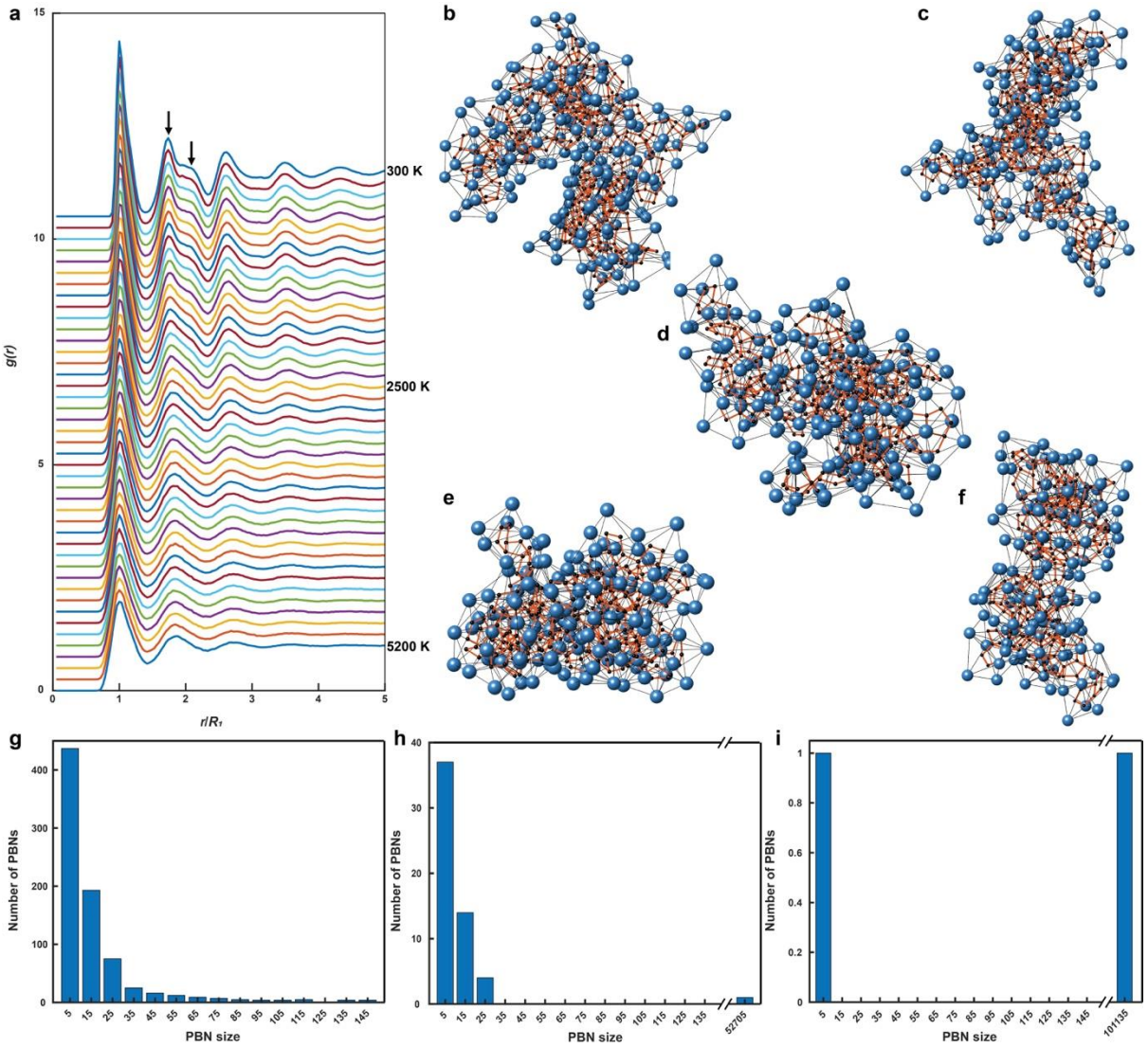

Extended Data Fig. 9 | Analysis of the molecular dynamics simulated Ta liquid. a, RDFs of the Ta structures during the quench from a liquid (5200 K) to a metallic glass state (300 K). At 5200 K, the RDF of the Ta liquid resembles those of the three experimental amorphous materials (Fig. 1c). At 300 K, the splitting of the 2nd and 3rd peaks in the RDF indicates the formation of the Ta metallic glass (arrows). **b-f**, Five largest PBNs in the MD simulated Ta liquid at 5200 K with 146, 132, 120, 118 and 105 pentagonal bipyramids, respectively. **g-i**, Number of PBNs as a function of the network size in the Ta structures at 5200K, 2500 K and 300 K, respectively. During the quench from a liquid to metallic glass state, the PBNs rapidly grow in size. At 300 K, a huge PBN is formed that extends to the entire Ta metallic glass.